J. Plasma Phys. (2024), *vol*. 90, 975900202
Published by Cambridge University Press

doi:10.1017/S0022377824000242

Development of a new magnetic mirror device at the Korea Advanced Institute of Science and Technology

D. Oh[1], M. Choe[1], G. Baek[1], D. Kim[1], B. K. Jung[2], K. J. Chung[3], I. Kourakis[4] and C. Sung[1],†

[1]Department of Nuclear and Quantum Engineering, Korea Advanced Institute of Science and Technology, Daejeon 34141, Republic of Korea

[2]Korea Atomic Energy Research Institute, Yuseong-gu, Daejeon 34057, Republic of Korea

[3]Department of Nuclear Engineering, Seoul National University, Seoul 08826, Republic of Korea

[4]Department of Mathematics, College of Arts and Sciences, Khalifa University of Science and Technology and Research, P.O. Box 127788, Abu Dhabi, United Arab Emirates

(Received 30 December 2023; revised 13 February 2024; accepted 14 February 2024)

A new magnetic mirror machine named KAIMIR (KAIST mirror) has been designed and constructed at the Korea Advanced Institute of Science and Technology (KAIST) to study mirror plasma physics and simulate the boundary regions of magnetic fusion plasmas such as in a tokamak. The purpose of this paper is to introduce the characteristics and initial experimental results of KAIMIR. The cylindrical vacuum chamber has a length of 2.48 m and a diameter of 0.5 m and consists of three sub-chambers, namely the source, centre and expander chambers. A magnetic mirror configuration is achieved by electromagnetic coils with a maximum magnetic field strength of 0.4 T at the mirror nozzles and 0.1 T at the centre. The source plasma is generated by a plasma washer gun installed in the source chamber with a pulse forming network system. The typical discharge time is ∼12 ms with a ∼6 ms (1–7 ms) steady period. Initial results show that the on-axis electron density at the centre is $10^{19–20}$ m^{-3} and the electron temperature is 4–7 eV. Two parameters were varied in this initial phase, the source power and the mirror ratio, which is the ratio of highest to lowest magnetic field strength in the mirror-confined region. We observed that the increase of the electron density was mitigated for a source power above 0.2 MW. It was also found that the electron density increases almost linearly with the mirror ratio. Accordingly, the stored electron energy was also linearly proportional to the mirror ratio, similar to the scaling of the gas dynamic trap.

Keywords: magnetic mirror, plasma devices, gas dynamic trap

1. Introduction

A magnetic mirror is an open magnetic system in a cylindrical geometry that suppresses longitudinal leakage through an axial mirror force exerted from the gradient of a magnetic

† Email address for correspondence: choongkisung@kaist.ac.kr

field along the parallel direction to the field (Post 1987; Dimov 2005; Ivanov & Prikhodko 2017). In comparison with conventional experimental nuclear fusion devices such as a tokamak, mirror machines have various attractive features. Due to their simple cylindrical geometry, construction costs for the chamber are less expensive, and interpretation of the physics becomes more straightforward than with toroidal systems. High-β plasma confinement, referring to a high ratio of plasma pressure to magnetic pressure, can be achieved in the mirror system, making mirror machines more economical. Moreover, current drive is not required for magneto-hydrodynamic (MHD) equilibrium, and therefore disruption-like events do not occur (Bagryansky *et al.* 2015). Removal of helium ash, a potential problem in commercial fusion reactor operation, is intrinsically possible from the open ends of the mirror machine. Despite these advantages, mirror systems also have certain shortcomings. First, mirror systems are not MHD stable in a simple mirror geometry (Rosenbluth & Longmire 1957); magnetic field lines become convex at the plasma boundary in a simple mirror system; and this geometry is vulnerable to the curvature-driven flute mode (Ivanov *et al.* 1994). Second, even though an axial mirror force is applied for mitigation, significant axial loss has been observed in this open magnetic system. Because of these disadvantages, the magnetic mirror is relatively less studied compared with other mainstream device concepts for fusion energy.

Nonetheless, the shortcomings of mirror systems have been mitigated through great efforts. For stability, a minimum-$|\boldsymbol{B}|$ (where |B| is the intensity of the magnetic field) field (Hastie & Taylor 1964) from the Ioffe bar (Ioffe & Kadomtsev 1970) and baseball coils (Moir & Post 1969) have been added to create a concave magnetic field in the entire region, which notably prevents fluctuations due to bad curvature. Moreover, it has been reported that the interchange instability, which arises from the bad curvature, can be significantly alleviated by stimulating vortex flow at the mirror nozzle through the application of a radial electric field (Yakovlev *et al.* 2018). For further reduction of axial loss, the tandem mirror concept from conventional mirror systems has been applied, which provides an ambipolar potential from the mirror plasma and an additional thermal barrier from heating (Baldwin & Logan 1979). Therefore, heating schemes have been developed, not only to increase the plasma temperature but also to enhance axial confinement. Thanks to these efforts, the magnetic mirror configuration has drawn more attention recently.

Currently, advanced studies are being performed to develop a fusion-based neutron source or a fusion reactor using mirror machines. Development of a continuously operating high-flux neutron source using a mirror plasma system is underway in a gas dynamic trap device with high-power ($\sim$50 MW) neutral beam injection (Bagryansky *et al.* 2020). To mitigate the axial confinement loss, several confinement schemes are being tested, including a helical mirror (Sudnikov *et al.* 2022) and multiple mirrors (Burdakov & Postupaev 2018). In addition, a mirror machine applying high temperature superconducting coils for high magnetic field intensity is under construction at the University of Wisconsin–Madison (Endrizzi *et al.* 2023).

Magnetic mirrors can also be utilized as a simulator of the boundary plasma in a tokamak. This is because the boundary plasma has relatively low temperature and its geometry, having a much longer axial length along the field line than its radial length, can be approximated as an open field system in a cylindrical geometry (Ohno 2017). Boundary plasma physics research has been conducted on several open magnetic field systems, including mirror machines, by simulating the plasma in the scrape-off layer region. Various experiments, including analysis of the detachment phenomena observed in many toroidal systems (Soukhanovskii 2017) and plasma–material interactions, have been performed with many mirror and linear devices such as the GAMMA10-PDX (Ezumi *et al.* 2019), NAGDIS-II (Ohno *et al.* 2001) and Pilot-PSI (Morgan *et al.* 2017).

https://doi.org/10.1017/S0022377824000242 Published online by Cambridge University Press

Here, we report a new magnetic mirror device developed at KAIST (Korea Advanced Institute of Science and Technology) called KAIMIR (KAIST mirror). It is planned to be utilized for fundamental plasma physics studies, such as on instabilities and turbulence, for future application as a neutron source or for fusion energy development. This machine will also be utilized to simulate a tokamak boundary plasma in order to improve our understanding of boundary plasma physics. Thus, both mirror and tokamak boundary plasma physics can be analysed with a relatively small device providing a flexible experimental set-up and dedicated fluctuation measurements.

To initiate plasma experiments with KAIMIR, we first constructed the chamber and developed a vacuum system. A simple mirror magnetic field was implemented using a magnetic field system. A copper magnetic coil was applied to generate a maximum axial magnetic field of ∼0.1 T at the centre and 0.4 T at the mirror nozzles. A plasma washer gun was utilized as the plasma source, and a probe system was utilized as the main diagnostic for electron density and temperature. The probe system includes a probe with sufficient negative-biased potential for ion saturation current measurements (I_{sat} probe) and a probe to measure the floating potential and electron temperature (sweeping probe). A data acquisition and control system was developed with LabView software to measure the diagnostic signals and control the power system. With these developed systems, we successfully discharged plasma and conducted an initial set of experiments.

In this study, we introduce the details of the KAIMIR system and its initial operation regime in terms of electron density and temperature. Section 2 presents the overall system, consisting of a chamber and vacuum system, magnetic field system, plasma source, diagnostics and data acquisition and control system. Section 3 reports the temporally and spatially measured results of the ion saturation current (I_{sat}), electron density and electron temperature in the reference condition. The trend of the various parameters and the radial profile change were analysed while varying the source power and the magnetic field configuration. Lastly, Section 4 summarizes our results and discusses future plans for advanced research.

2. Description of the magnetic mirror system, KAIMIR

2.1. *Chamber and vacuum system*

The computer-aided design model of the vacuum chamber of the KAIMIR is introduced in figure 1. The overall geometry of the device is a cylinder with a diameter of 0.5 m and a length of 2.48 m. The material of the chamber is stainless steel 316L. The vacuum chamber consists of source, centre and expander chambers with two mirror nozzles connecting them. The source chamber has a diameter of 500 mm and a length of 450 mm. In this chamber, the plasma source is installed and a single turbomolecular pump and gas injection lines are connected for pressure control. The centre chamber has a diameter of 500 mm and a length of 1180 mm. Plasma confinement in the magnetic mirror geometry takes place in this chamber. The expander chamber has the same size as the source chamber. In the expander chamber, an identical turbomolecular pump as in the source chamber and a tungsten collector plate to dump the source plasma are installed. Both the plasma source and collector plate are designed to be movable along the axial direction to adjust the stability condition of the interchange mode (Nagornyj, Ryutov & Stupakov 1984). All chambers are installed on a rail to fabricate and modify the system conveniently.

To generate a high vacuum for plasma experiments with low impurities, as mentioned above, two identical turbomolecular pumps with a volume flow speed of 2000 l s^{-1} for He are installed at the bottom of the source and expander chambers. Both pumps are connected to a single rotary vane pump. Vacuum pressure is measured with various vacuum gauges

https://doi.org/10.1017/S0022377824000242 Published online by Cambridge University Press

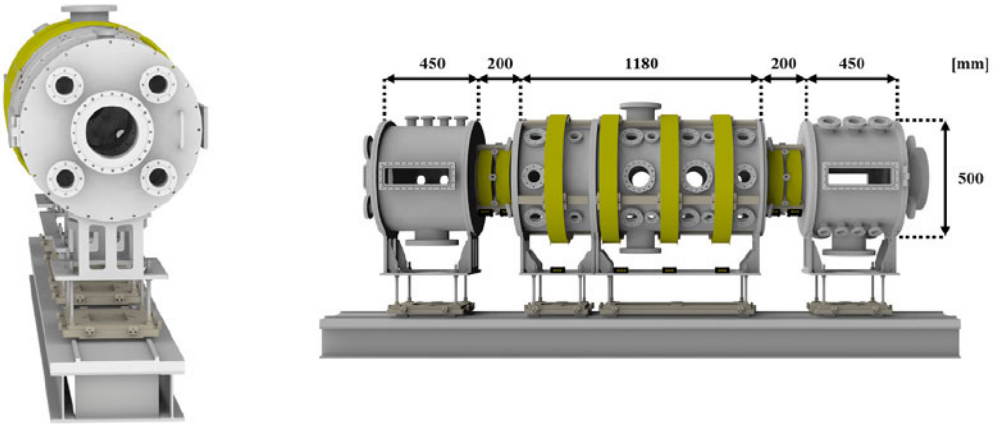

FIGURE 1. Computer-aided design model of the vacuum chamber.

in each chamber. A set of convection gauge and capacitance manometer is applied for low vacuum ($\geq 10^{-4}$ Torr) to atmospheric pressure measurements, and the high vacuum condition ($< 10^{-4}$ Torr) is monitored through ion gauges located on each chamber. The base pressure is $\sim 2.0 \times 10^{-7}$ Torr within this vacuum system.

2.2. *Magnetic field system*

The magnetic field in this device is generated through two kinds of electromagnetic coils, mirror coils and solenoid coils. Specification of the coils is shown in table 1. Two insulated-gate bipolar transistor (IGBT) switches are installed to control each coil module. By connecting the switches in parallel, the applied power to the switches can be divided. Schematic of the circuit for coil power system is introduced in figure 2*(a)*.

The designed magnetic field is calculated using elliptic functions (Derby & Olbert 2010). Figure 2(*b*) shows the contour of the expected magnetic field intensity in typical experimental conditions with $B_z \sim 0.35$ T at the mirror nozzles and $\sim$0.088 T at the centre along the $R = 0$ line or on-axis, corresponding to an applied current of 168 A and 116 A to the solenoid and mirror coils, respectively. We verified the magnetic field system by measuring the axial profile of the magnetic field (B_z) at $R = 0$. Figure 2(*c*) shows that the measured and calculated profiles are well matched within their uncertainties, indicating a proper fabrication and installation of the magnetic field system. From the simulation of the radial profile of B_z, the field intensity is radially uniform and the magnetic ripple is negligible (ripple $\equiv \delta B_{\text{ripple}}/B_0 \leq 0.03$) in the $R < 100$ mm region, where most of the plasma exists during discharge. Therefore, we do not expect instabilities driven by the magnetic ripple at the edge region in this device.

2.3. *Plasma source*

As a high-density pulsed plasma source, a plasma washer gun is utilized (Fiksel *et al.* 1996) in this device. The gun is mounted with a stainless steel pipe in the source chamber, and its axial position can be adjusted through a linear guide motion structure. The gun plasma is generated inside a washer ring between a hollow cathode and anode and then discharged to the collector plate in the expander chamber, generating a plasma column along the centre of the chambers.

Figure 3 exhibits an electrical circuit schematic of the components related to the plasma source. The source plasma in the washer gun is mainly sustained by power from a pulse

https://doi.org/10.1017/S0022377824000242 Published online by Cambridge University Press

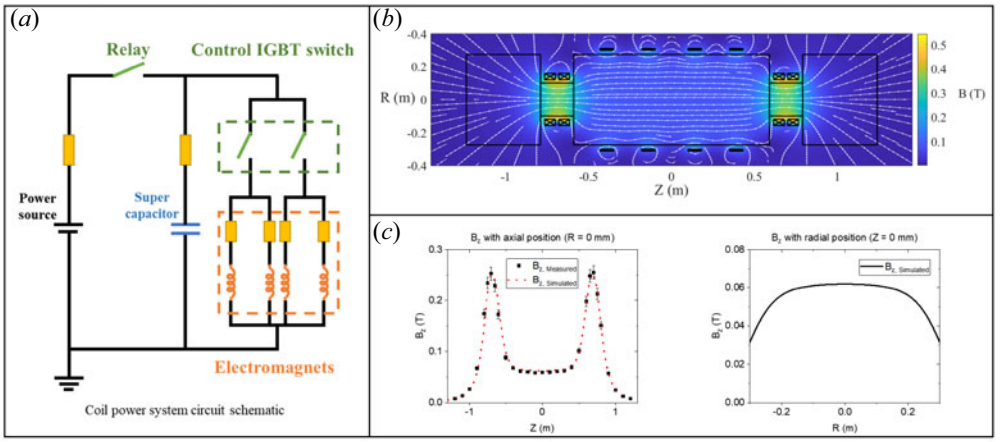

FIGURE 2. (*a*) Coil power system schematic. (*b*) Simulation of the magnetic field in the *R*–*Z* plane in the reference condition ($B_z \sim 0.088$ T at centre, ~0.35 T at the mirror nozzle with the solenoid coil current 168 A, mirror coil current 116 A). (*c*) Simulated and measured B_z by axial position at $R = 0$ mm and simulation result of B_z by radial position.

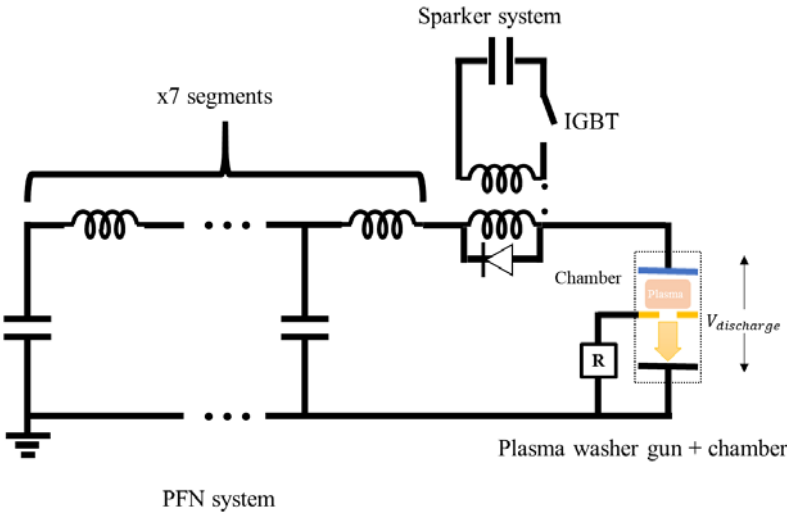

FIGURE 3. Electrical circuit schematic of the PFN, sparker system and plasma source.

forming network (PFN) system. The PFN system can provide flat, square power to the load (Rose 2015). The PFN used in this study consists of seven segments of capacitor and inductor components. Each segment has a 1.28 mF capacitor and 0.32 mH inductor, connected in series, both connected in a ladder shape in a Guillemin type E (Rathod *et al.* 2014). The total characteristic impedance of the PFN system is 0.5 Ω and the pulse duration is 8.96 ms, calculated from the overall capacitance and inductance values.

To initiate the plasma discharge, a sparker system generates a high-voltage spark between the gun cathode and anode. The high potential required for initial plasma breakdown is applied through a 1 : 3 transformer from the sparker capacitor. Since the potential required for sustaining a discharge is lower than the potential required for initial

https://doi.org/10.1017/S0022377824000242 Published online by Cambridge University Press

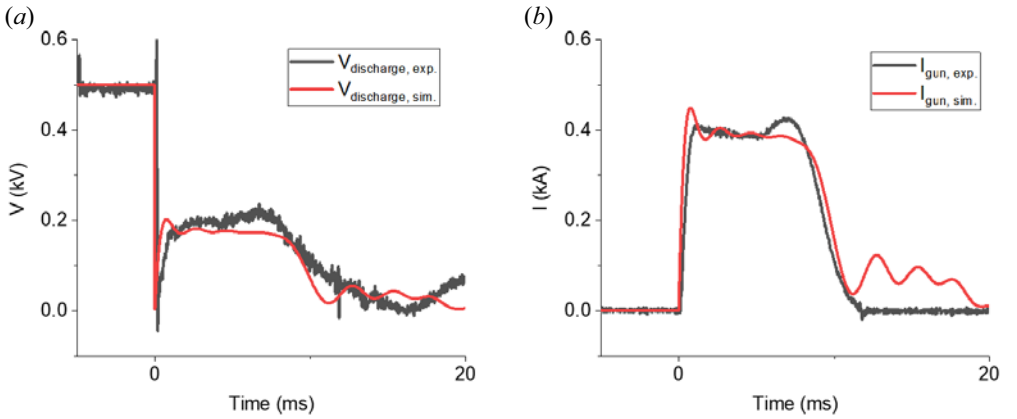

FIGURE 4. Temporal evolution of (*a*) discharge voltage and (*b*) gun current in the reference condition experiments and circuit simulation.

breakdown, the PFN system can be operated at a lower potential than required for initial breakdown with the sparker system.

Helium is used as the main discharge gas in the experiments. The discharge gas is injected for 100 ms right before plasma breakdown through a piezoelectric valve installed on the gas line in front of the plasma washer gun. The gas throughput of the valve is controlled by a maximum 100 V applied voltage from 0 to 525 sccm. The pressure at the front side of the piezoelectric valve is fixed to 3.5 bar and controlled with a pressure-regulating valve. The injection timing and duration are adjusted by the trigger signal from the data acquisition and control system, which is described in § 2.5.

Figure 4 shows the temporal evolution of the voltage and current in the PFN circuit applied to the washer gun under the reference discharge condition. After ramp up in ∼1 ms after the triggering of the sparker, the voltage and current applied to the plasma gun are maintained until ∼4 ms. Afterwards, a small hump in the signal with a height of ∼10 % is observed in both voltage and current signals from 4 to 7 ms. After 7 ms, the voltage and current signals start to decay and fall off to 0 at ∼12 ms. The measured values are compared with the circuit simulation results, as shown in figure 4. The signal levels during the steady period (1–4 ms) agree well, indicating that the PFN system works as designed. However, some discrepancies remained. In the simulation, the gun current fluctuates in contrast to the experiment. This is because we simply assumed the load as a resistor. In the experiment, the circuit is opened when the plasma is turned off, so the current flow becomes 0. Then the discharge voltage shows ringing in the experiment, dissipating the remaining energy in the PFN circuit. Also, the circuit simulation does not predict the hump observed in the experiment in the 4–7 ms period. This difference can be attributed to the impedance mismatch between the PFN circuit and the plasma in time. Different rise and fall times can be related to slight differences in the estimated stray resistance.

2.4. *Langmuir probe system*

A Langmuir probe is a versatile tool that can measure the electron density, electron temperature and electron energy distribution from the characteristics of the current flowing from the plasma to the metal probe tip under arbitrary biased voltage (Chen 2003). Cylindrical Langmuir probes were fabricated to measure I_{sat} at a fixed negative voltage and to acquire current–voltage (I–V) curves by sweeping the biased voltage for electron temperature measurements.

https://doi.org/10.1017/S0022377824000242 Published online by Cambridge University Press

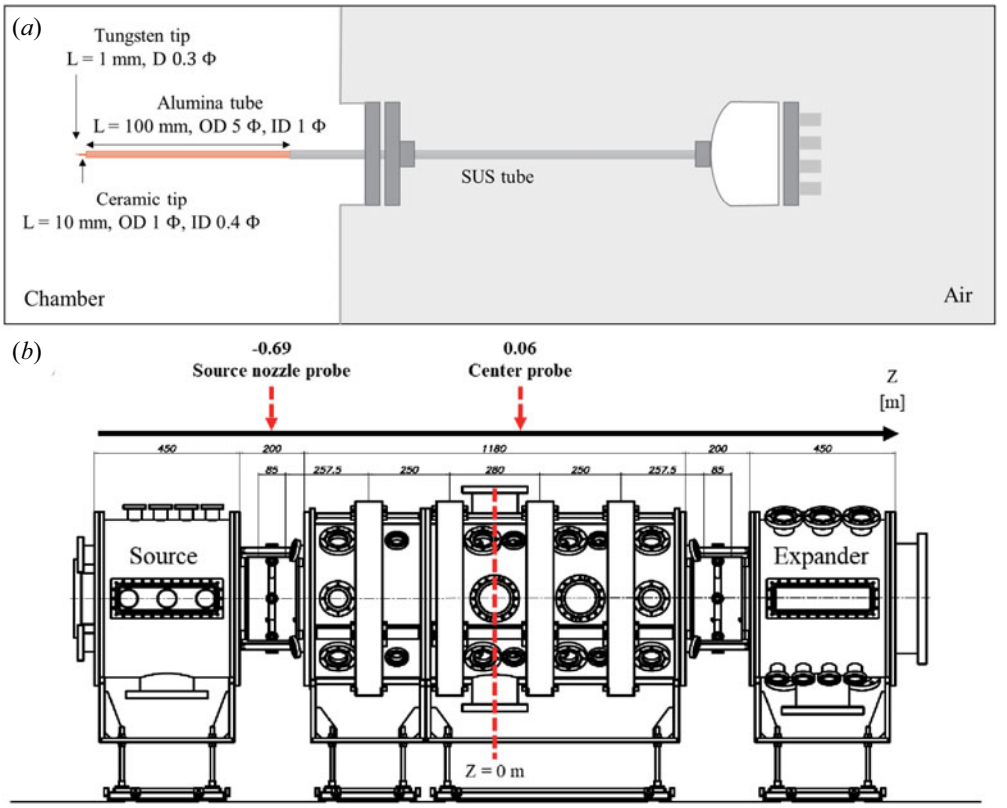

FIGURE 5. (*a*) Drawing of the Langmuir probe structure. (*b*) Axial locations of the probe measurements.

The structure of the Langmuir probe consists of a tungsten metal tip, alumina tube, ceramic tip and a stainless steel 316L (SUS316L) tube, as shown in figure 5(*a*). The alumina and SUS316L tube, used to sustain the structure and protect the wire from the plasma, are connected mechanically. The length of the tungsten tip exposed to the plasma is ∼1 mm, with a diameter of 0.3 mm. Figure 5(*b*) shows the axial locations of the probes used in this study. Probe measurements are performed mostly near the centre of the system, $Z \sim 0.06$ m. We also inserted a probe at the mirror nozzle near the plasma source to monitor changes in the source region, $Z \sim -0.69$ m, during the experiment.

The value of I_{sat} is monitored by measuring the probe current with a negative-biased voltage sufficient for ion saturation current measurements. A bias voltage of −150 V is supplied in most cases by a linear DC power supply, which is determined from current measurements from the sweeping probe. The value of I_{sat} is measured by using a shunt resistor and isolation amplifier, as shown in figure 6(*a*). To acquire the I–V characteristic curve for electron temperature measurements in the sweeping probe circuit, a voltage amplifier is added, as shown in figure 6(*b*). A triangular waveform with a 10 kHz sweeping frequency is generated from a developed data acquisition and control (DAC) system for voltage sweeping, and it is amplified through the voltage amplifier with a gain as high as 10. The probe current with the swept voltage is measured by the shunt resistor, as used in the I_{sat} measurements. The swept voltage is monitored by 1 : 10 probe. In the time trace of the voltage and current, the triangular waveform of the swept voltage became

https://doi.org/10.1017/S0022377824000242 Published online by Cambridge University Press

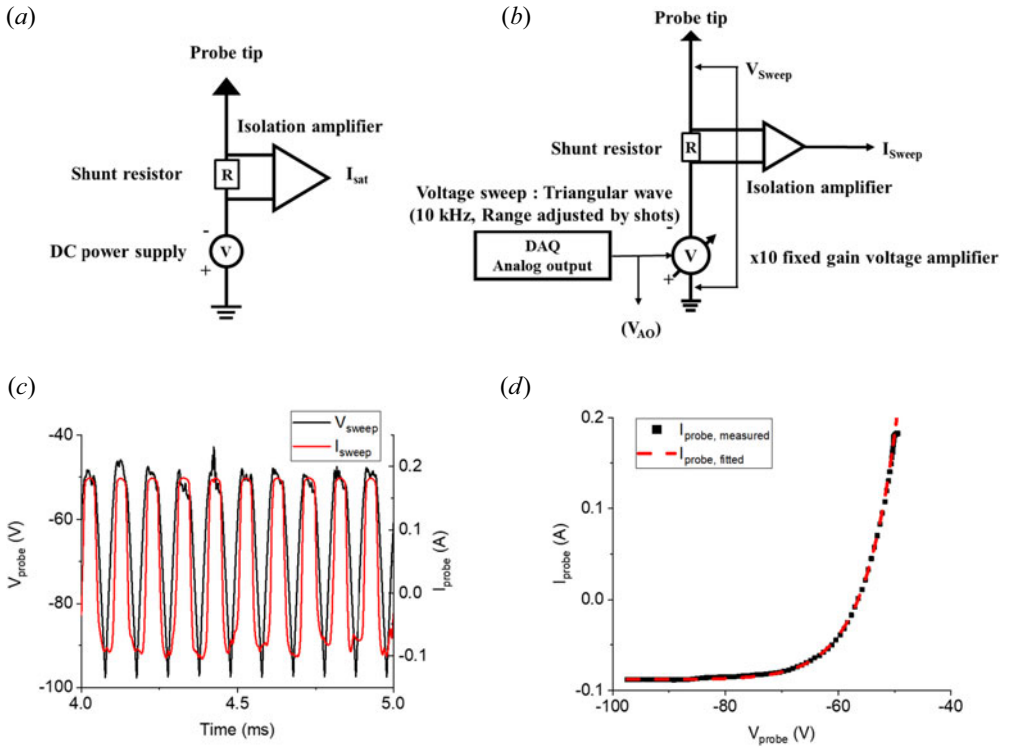

FIGURE 6. Panels show (*a*) I_{sat}, (*b*) sweeping probe circuit schematics, (*c*) sample voltage and current time traces and (*d*) I–V curve.

distorted when the probe current reached the limitation of the voltage amplifier, as shown in figure 6(*c*), because of the high plasma density. Because of this limitation, the I–V curve was obtained in the ion saturation region and transition to the electron saturation region. To remove the possible distortion of the I–V curve in the transition region, we excluded the distorted points in the fitting of the I–V curve. Electron temperature is estimated by averaging the values from 10 I–V curves. We can notice that the resulting I-V curve follows the exponential fitting properly, as shown in figure 6(*d*). From the estimated electron temperature and measured I_{sat}, the electron density is estimated from the Bohm formula, $n_e = I_{sat}/e^{-0.5}A_p q_e\sqrt{kT_e/M_{ion}}$, where e is base of the natural logarithm, A_p is area of the probe surface, q_e is electric charge of electron, T_e is electron temperature and M_{ion} is mass of the ion (Chen 2003). We note that the Bohm formula is valid for a planar probe, as the ion current does not saturate in the cylindrical probe due to the sheath expansion from the bias voltage, since total sheath thickness is $d = [\frac{2}{3}(2q_eV_0/kT_e)^{3/4} + 5]\lambda_{Debye}$, where d is sheath thickness, V_0 is voltage between probe and plasma and λ_{Debye} is Debye length. However, since the measured electron density is high ($>10^{19}$ m^{-3}) in our system, the ratio of the probe size to the Debye length, $\xi_p(= r_p/\lambda_{Debye})$ with probe radius, r_p, is sufficient (exceeding >56) to use the Bohm formula where the Laframboise curve shows saturating trends for the bias voltage (Chen 2001). Based on this estimate, the Bohm formula was utilized in this study. However, it is noteworthy that the I_{sat} level can still be overestimated by 60 % due to the sheath expansion at relatively low density ($<10^{19}$ m^{-3}). We therefore need to perform an additional analysis to interpret I_{sat} measurements when the plasma density is low.

https://doi.org/10.1017/S0022377824000242 Published online by Cambridge University Press

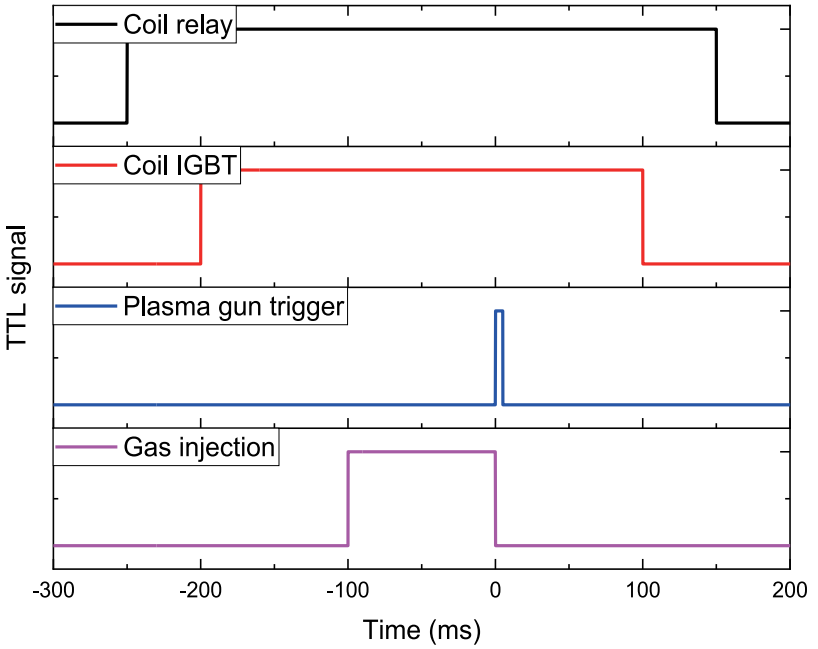

FIGURE 7. Specific trigger signals with time to control the magnetic coils, plasma gun and gas.

2.5. *Data acquisition and control system*

We developed the DAC system for triggering and controlling the power systems and acquiring the diagnostic signals based on LabView software. Specific timings of the triggering for diagnostics and control are shown in figure 7. The digital output signal from the DAC is converted to an optical signal in an electro-optic transceiver for electrical isolation of the power and signal lines. This system also synchronizes and controls the on/off timing of the relay and the IGBT switches in the coil power system, the IGBT switch for the sparker system and the piezoelectric valve in the gas injection system. Voltage and current measurements to monitor the PFN and coil power systems are performed with a relatively low sampling rate, 0.1 MS s^{-1} ($=0.1\times10^6$ samples per second) and Langmuir probe signals are measured with a relatively high sampling rate, 2.0 MS s^{-1}.

3. Results of the initial plasma experiments with the KAIMIR system

We initially investigated the fundamental plasma parameters and the operation regime of He discharges in KAIMIR. We verified that the discharge is reproducible within 10 % by measuring the on-axis I_{sat} at $Z\sim0.06$ m, where $Z=0$ is the axial centre of the system, as shown in figure 5(*b*), in the reference discharge condition, which is explained in the following section. Using the reproducibility of the discharge, spatial profile measurements were performed in a shot-by-shot basis.

3.1. *Characteristics of the plasma in the reference discharge condition*

The reference discharge condition refers to the typical discharge conditions in KAIMIR experiments, defined as the following adjustable system variables: magnetic field configuration, PFN voltage, sparker voltage, gun location and gas injection timing and duration. The reference condition is summarized in table 2. We first investigated the characteristics of the plasma generated in the reference condition.

https://doi.org/10.1017/S0022377824000242 Published online by Cambridge University Press

	Mirror coil	Solenoid coil
Coil resistance	1.026 Ω	0.746 Ω
Coil inductance	43.07 mH	15.31 mH
Rise time (L/R)	41.98 ms	20.52 ms
Number of turns	360	120
Coil diameter	278 mm	620 mm
Coil weight	15.1 kg	10.9 kg
Installed location	±645 mm / ±730 mm	±138 mm / ±388 mm

TABLE 1. Specifications of the mirror and solenoid coils.

Variable	Estimated value	Available value
Magnetic field intensity (T)	0.35 at mirror 0.088 at centre	0–0.4 at mirror 0–0.1 at centre
Base pressure (Torr)	$\sim 2.0 \times 10^{-7}$	$> 2.0 \times 10^{-7}$
PFN voltage (kV)	0.5	0–1
Trigger voltage (kV)	3.5–4.0	0–4
Gas species	Helium	Helium, Argon
Gas throughput (sccm)	∼490	0–500
Gas injection timing (ms)	−100 to 0	—
Axial position of the source (m)	−0.9	−1.1–−0.6
Axial position the collector plate (m)	1.0	1.0–1.2

TABLE 2. System variables for the reference condition and their ranges in the KAIMIR experiments. The trigger timing of the IGBT switch for the sparker system is referenced as 0 ms, and the centre of the vacuum chamber is referenced as the 0 m axial position.

In the reference condition, magnetic field amplitudes were set to 0.088 T and 0.35 T at the centre and mirror nozzles, respectively. Thus, the mirror ratio, defined as the ratio of maximum and minimum magnetic fields in the mirror plasma, is around 4 in this condition. The PFN voltage for the reference condition was set to 0.5 kV, the middle of the adjustable voltage range (0–1 kV). Trigger voltages were set to sufficient levels for initial breakdown, varying from 3.5 to 4.0 kV. We confirmed that variation in the trigger voltage did not affect the plasma performance. Gas throughput and injection timing were set to 490 sccm from −100 to 0 ms, where 0 ms refers to the time when the plasma starts to discharge by applied trigger voltage. Axial positions of the source and collector plate were fixed to $Z = -0.9$ m and 1.0 m, respectively.

Figure 8 shows the temporal evolution of the source power (PFN power) and probe measurement results including I_{sat}, electron density and electron temperature. It can be noticed in figure 8(*a*) that steady power is supplied to the plasma gun during discharge, as expected from figure 4. After triggering, PFN power was maintained until ∼4 ms, after which it slightly increased during 4–7 ms. After 7 ms, the power decayed to 0 by ∼12 ms. Figure 8(*b*) shows I_{sat} measured by the probe located on-axis ($R = 0$, $Z = 0.06$ m). The current was low pass filtered (f_{cutoff}: 10 kHz) to see the trend of the parameters. We also observed the floating potential measured by the sweeping probe at the same location. The values of I_{sat} and floating potential stayed at ∼0.05 A and −58 V, respectively, during 1–7 ms. After 7 ms, I_{sat} decreased exponentially, following the decay of the source power. The

https://doi.org/10.1017/S0022377824000242 Published online by Cambridge University Press

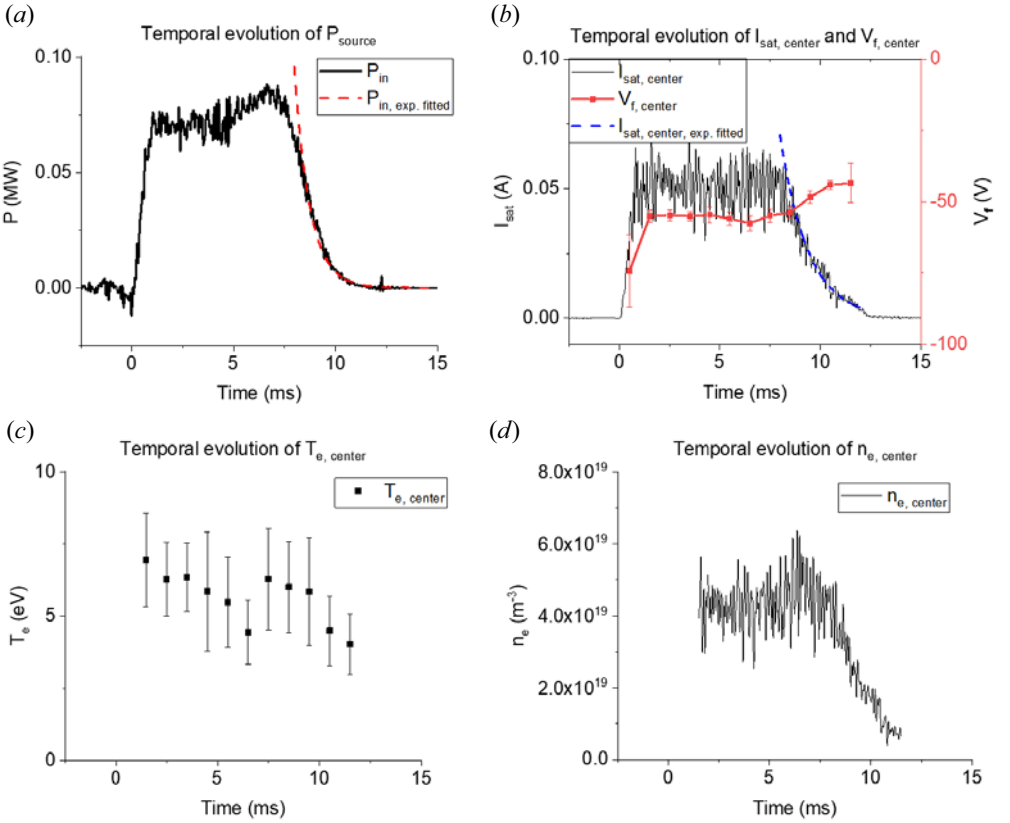

FIGURE 8. Temporal evolution of (*a*) source power, (*b*) I_{sat}, floating potential (V_f), (*c*) electron temperature (T_e) and (*d*) electron density (n_e) on-axis ($Z = 0.06$ m) in the reference condition.

absolute value of the floating potential was also reduced in this period; this reduced value could be due to the reduced seeded electrons from the gun at lower PFN powers. The electron temperature measured by the sweeping probe was ~4–7 eV during 1–7 ms, as shown in figure 8(*c*). Based on I_{sat} and the electron temperature, we estimated the electron density. As shown in figure 8(*d*), the density level was $\sim 4.5 \times 10^{19}$ m^{-3} in the same time range (1–7 ms). In the decay phase (>7 ms), the reduction of I_{sat} was mainly due to changes in the electron density, rather than the electron temperature, since it was observed that the density was reduced more abruptly than the temperature. It is also worth noting that the decaying slope of the PFN power is steeper than the slope of I_{sat} or electron density. Applying exponential fitting ($\sim C_1 exp(-t/\tau_{decay}) + C_2$) in the 8–11 ms decay phase, we observed that the characteristic decay time (τ_{decay}) of the power is ~0.6 ms while the decay time of I_{sat} is ~1.6 ms. Considering the possible overestimation of the I_{sat} level due to the sheath expansion at low density, the exact decay time of I_{sat} can be shorter than the obtained level. The estimated time considering this effect is ~1.4 ms, which is still longer than the decay time of the power. This difference shows that the plasma was sustained even after the power was turned off, which could represent the confinement efficiency.

From the on-axis electron density and temperature of the plasma, the main physical parameters of the plasma were estimated as shown in table 3. Operation pressure is the neutral pressure during the discharge, and it was estimated under the assumption of a uniform pressure inside the chamber with the equation $Q = V_{chamber}(dP_{chamber}/dt) = Q_{gas\ injection} - P_{chamber}S_{pump\ speed}$, where $V_{chamber}$ is the overall volume of the vacuum

https://doi.org/10.1017/S0022377824000242 Published online by Cambridge University Press

Parameter	Estimated value
Electron density (m^{-3})	4.5×10^{19}
Electron temperature (eV)	6
Operation pressure (mTorr)	0.95
Neutral density (m^{-3})	3.1×10^{19}
Debye length (mm)	0.0027
Electron Larmor radius (mm)	0.067
Ion Larmor radius (mm)	1.8
Electron gyrofrequency (MHz)	2450
Ion gyrofrequency (MHz)	0.332
Electron plasma frequency (MHz)	60 200
Ion plasma frequency (MHz)	704
Ion bouncing frequency (MHz)	0.00135
$\nu_0^{e/i}$ (MHz)	96.6
$\nu_0^{i/i}$ (MHz)	25.2
$\nu_0^{e/n}$ (MHz)	2.15
$\lambda_{\mathrm{mfp}}^{e/i}$ (mm)	10.7
$\lambda_{\mathrm{mfp}}^{i/i}$ (mm)	0.149
$\lambda_{\mathrm{mfp}}^{e/n}$ (mm)	479
Electron thermal velocity (km s^{-1})	1030
Ion thermal velocity (km s^{-1})	3.79
Sound velocity (km s^{-1})	12.0
Alfven velocity (km s^{-1})	142

TABLE 3. Main plasma parameters in the reference condition. Here, $\nu_0^{s/s'}$ is the collision frequency from species s to s', and $\lambda_{\mathrm{mfp}}^{s/s'}$ is the mean free path of collision from species s to s'.

chamber, $Q_{\mathrm{gas\ injection}}$ is the flow rate of the gas injection line and $S_{\mathrm{pump\ speed}}$ is the total pumping speed of the pump system. The calculated pressure was 0.95 mTorr, which is in accordance with the measured pressure by ion gauge ($\sim$1 mTorr). This pressure corresponds to the neutral density $3.1 \times 10^{19}\,\mathrm{m}^{-3}$ at room temperature. Because ion temperature measurements are not available at this point, T_i was assumed to be 10 % of T_e from previous studies performed under similar conditions, including electron density and temperature levels, and thus a similar energy transfer rate from electrons to ions by collision (Thakur *et al.* 2016; Arakawa *et al.* 2019). As the ion and electron Larmor radii are much smaller than the scale of the current system, the plasma was magnetized in these initial experiments. The electron–ion and ion–ion collision frequencies are high enough to satisfy the condition, $L \gg \lambda_{\mathrm{ii}}(\ln R_M/R_M)$, which indicates that the KAIMIR plasmas are in the gas dynamic regime (Ivanov & Prikhodko 2017). Based on the estimated neutral pressure, the electron–neutral collision frequency ($\nu_0^{e/n}$) and its mean free path ($\lambda_{\mathrm{mfp}}^{e/n}$) were also calculated based on the electron–neutral total cross-section data (Raju 2018). As collisions of electrons with ions and electrons lead to the diffusion of the electrons, collision events with neutrals also play a role in the diffusion. However, based on the comparison of collision frequencies, electrons will be diffused mainly by the collisions with the charged particles.

https://doi.org/10.1017/S0022377824000242 Published online by Cambridge University Press

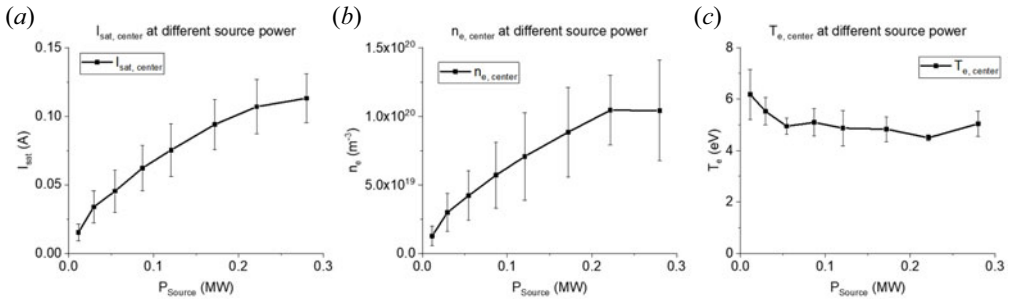

FIGURE 9. Panels show (*a*) $I_{\rm sat}$, $R = 0$ mm, $Z = 0.06$ m, (*b*) n_e and (*c*) T_e with varying source power. The data are averaged in the range 4–7 ms.

3.2. *Effect of source power*

To check the operation regime, the on-axis electron density and temperature of the plasma at $Z \sim 0.06$ m were measured while scanning the source power (PFN power). In this experiment, the source power was varied by adjusting the PFN voltage from 0.2 to 0.9 kV.

Probe measurements were done at $(R, Z) = (0, +0.06\ \text{m})$. Figure 9(*a*) shows the changes in $I_{\rm sat}$ with the source power. The $I_{\rm sat}$ level increased with the source power and its growth was alleviated with the source power. As shown in figures 9(*b*) and 9(*c*), we observed that the electron density increased from 1.3×10^{19} to $1.0 \times 10^{20}\ \text{m}^{-3}$ while the electron temperature remained at a similar level of 5–6 eV during the power scan. It is noteworthy that the increase of the electron density level was mitigated at high source power, over 0.2 MW, similar to the behaviour observed in the $I_{\rm sat}$ measurements. Therefore, the trend observed in $I_{\rm sat}$ was mainly attributed to changes in the electron density with source power.

The similar levels of electron temperature observed during the power scan experiment can be explained by the plasma generation mechanism in KAIMIR. Plasma in this device is mainly generated from collisions between background neutrals and electrons emitted from the washer gun. The electron–neutral impact ionization cross-section from the ground has a threshold at 24.6 eV and rapidly increases with higher electron temperature (Ralchenko *et al.* 2008). It is expected that ionization of the background plasma is driven by the tail of energetic electrons or via multiple successive impact excitations. Because the density and temperature of the initial seed electrons increase at higher source power, the ionization rate affecting the density of the main plasma increases. However, to increase the electron temperature of the main plasma, the energetic electrons from the gun should be thermalized through Coulomb collisions with the background electrons. Since the Coulomb collision frequency with the energetic electrons is inversely proportional to cube of the velocity of energetic electrons from the gun, higher source power can be ineffective in increasing the temperature of the background electrons.

Radial profiles of the electron density and temperature were measured at PFN voltages of 0.3, 0.5, 0.7 and 0.9 kV in the range $R = 0$–50 mm. The electron density over all radial positions increased with the source power. It also tends to decrease as it moves radially outward. Here, electron density could be overestimated at the periphery region ($R > 30$ mm) similar to the decaying phase in § 3.1, which will make the profile steeper than the measured one. The density profile was fitted with a Cauchy distribution ($n_e(r) = (2A/\pi)(w/(4r^2 + w^2))$) to evaluate the effective radius of the plasma. In the fitting, the characteristic length of the radial profile (w) increased by 20 % while varying the source power from 0.03 to 0.28 MW. This demonstrates that the radial profile broadens as the

https://doi.org/10.1017/S0022377824000242 Published online by Cambridge University Press

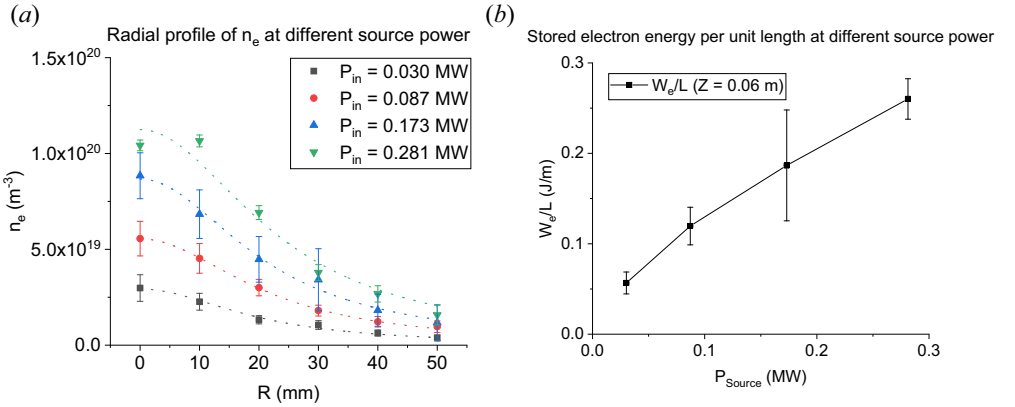

FIGURE 10. (*a*) Radial profile of n_e with the measured data and the fitted curve (dashed line) with a Cauchy distribution, and (*b*) the stored electron energy at $Z = 0.06$ m with varying source power.

source power increases. Stored electron energy per unit length at $Z = 0.06$ m, which refers to the integrated energy density over the area in this study, was calculated from these profiles to estimate the trend of overall stored energy of the plasma. To calculate the stored electron energy, the radial profiles of the electron density and temperature were integrated with assumed azimuthal symmetry, $W_e/L = 2\pi \int_0^R \frac{3}{2} n_e k_B T_e r \, \mathrm{d}r$, as shown in figure 10(*b*). In this estimation, R, the plasma radius, was determined to be 50 mm. The slope of the stored electron energy decreases as the source power increases, consistent with the trend of n_e observed in figure 9(*b*). The estimated energy can be decreased up to 30 % considering the overestimation of the probe due to sheath expansion. However, the observed trend will still be valid since this effect is more significant for the case with the lower source power.

The decrease of the slope of the stored electron energy represents the fact that the stored energy of the plasma does not follow the source power linearly. This trend can be attributed to the reduced confinement time with the source power. If higher source power increases the ion temperature of the plasma, this will reduce the axial confinement time, according to the gas dynamic trap scaling, $\tau_{\mathrm{GDT}} \sim R_M L / V_s$. It is also possible that radial transport is enhanced with the source power due to a certain instability. Further investigation will be performed to understand the observed trend.

3.3. *Effect of the mirror ratio*

The mirror ratio is known to affect axial confinement significantly in mirror machines (Soldatkina, Bagryansky & Solomakhin 2008). In the present work, the magnetic field intensity at the mirror nozzles increased from 0.14 to 0.35 T while the field intensity at the centre ($Z = 0$) remained at 0.07 T, as shown in figure 11(*a*). Consequently, the mirror ratio of the system varied from 2 to 5. During the scan, the source power was maintained to 0.87 MW. To check the changes in the source region by the magnetic field intensity at the mirror nozzle between the source and centre chambers, we observed the trend of I_{sat} at the source nozzle near the plasma gun. As shown in figure 11(*b*), $I_{\mathrm{sat,source\ nozzle}}$ is almost constant at different mirror ratios, while $I_{\mathrm{sat,centre}}$ increases with the mirror ratio. This indicates that the increased $I_{\mathrm{sat,centre}}$ is not due to changes in the source region. Figures 11(*c*) and 11(*d*) show the variations in the electron density and temperature with the mirror ratio. The electron density increases almost linearly with the mirror ratio, which could be related to enhanced confinement due to the reduction of axial leakage at higher mirror ratios.

https://doi.org/10.1017/S0022377824000242 Published online by Cambridge University Press

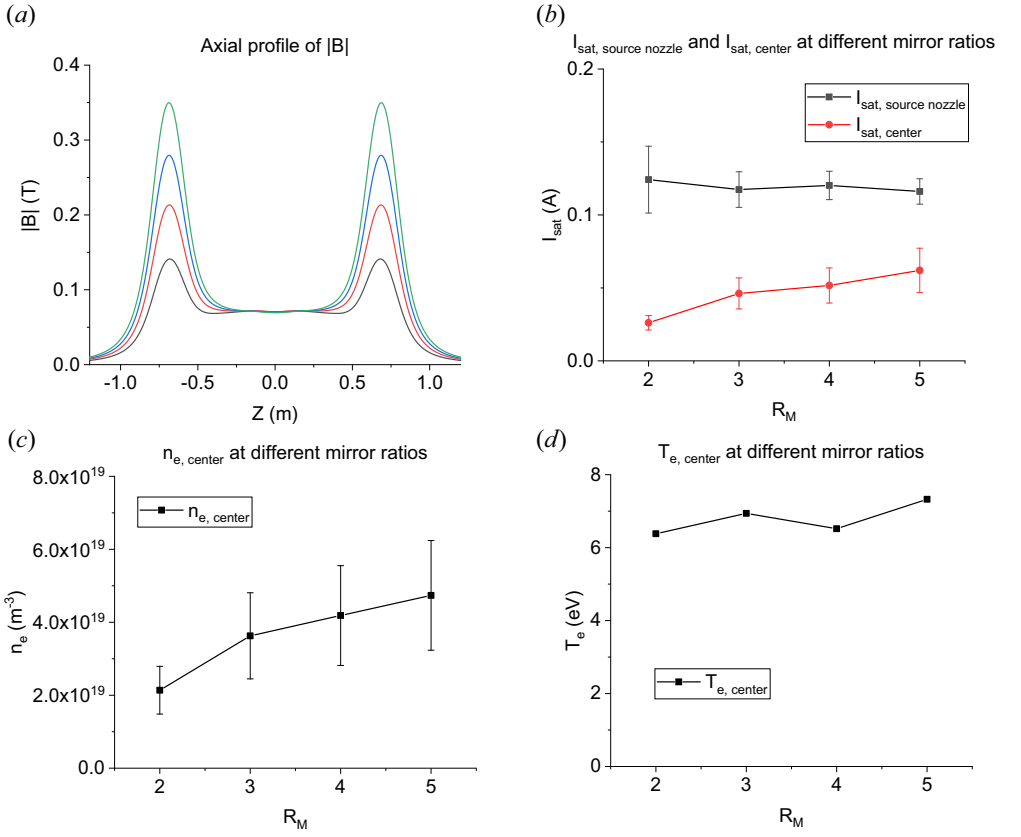

FIGURE 11. (*a*) Axial profile of the magnetic field intensity for mirror ratios of 2–5, (*b*) $I_{\mathrm{sat,sourcenozzle}}$ and $I_{\mathrm{sat,centre}}$, (*c*) n_e and (*d*) T_e on-axis at different mirror ratios (R_M). The data are averaged in the range 4–7 ms.

Figure 12(*a*) shows the radial profiles in the mirror ratio scan experiment. Results show that electron density increases with the mirror ratio at all radial locations. The density profile was fitted with the same Cauchy distribution used in the power scan analysis (§ 3.2). The characteristic length of the radial profile remained within values below 10 %, which indicates that the shape of the radial profile was almost constant while varying the mirror ratio. The same calculation process performed in the source power scan was applied to calculate the stored electron energy. It was found that the stored electron energy almost linearly increased with the mirror ratio, as shown in figure 12(*b*). This trend was also identical when the sheath expansion is considered in the probe measurements. The linear increase of the stored electron energy with mirror ratio while maintaining the source power suggests that the plasma confinement is enhanced with the mirror ratio. This trend is consistent with the confinement time scaling in the gas dynamic regime, $\tau_{\mathrm{GDT}} \sim R_M L/V_s$, which can be expected from the high collision frequencies shown in table 3.

4. Summary and future work

A new linear magnetic mirror device called KAIMIR was constructed and initial experiments were conducted. In the device, plasma is generated in pulsed mode with a plasma washer gun and a mirror geometry magnetic field is generated from a coil power

https://doi.org/10.1017/S0022377824000242 Published online by Cambridge University Press

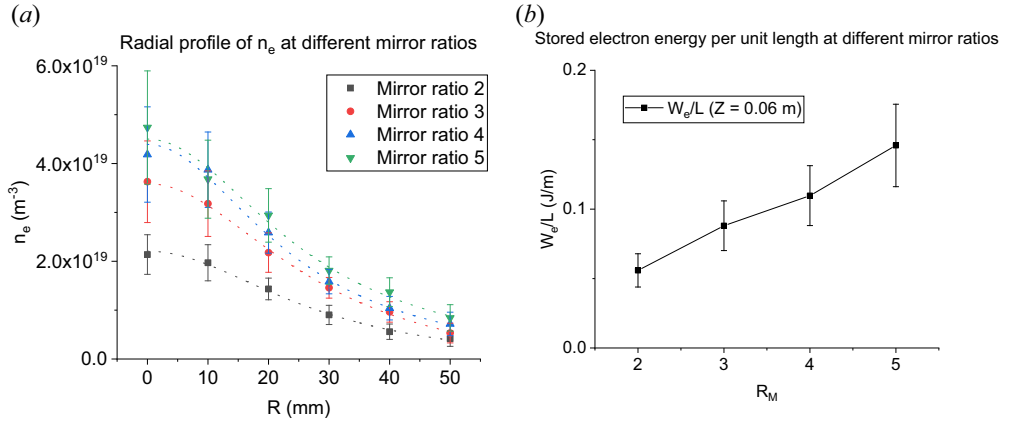

FIGURE 12. (*a*) Radial profile of n_e with the measured data and the fitted curve (dashed line) with Cauchy distribution, (*b*) the stored electron energy at $Z = 0.06$ m for different mirror ratios (R_M).

system. The maximum magnetic field intensity is 0.1 T at the centre and 0.4 T at the mirror nozzles. The source power of the plasma gun is supplied by a PFN system with a duration of ∼10 ms. Data acquisition of diagnostics as well as system triggering and synchronization are performed with a DAC system. Through a series of initial experiments, we measured the electron density and electron temperature in diverse conditions and determined the possible range of electron density and temperature levels in this system. The on-axis electron density could vary from 1.3×10^{19} to 1.0×10^{20} m^{-3} and the electron temperature in the range 4–7 eV by the source power. These values are in a similar range to those of other devices used to conduct edge plasma physics studies (Ohno 2017). The electron density also linearly increases with the mirror ratio, consistent with gas dynamic trap scaling. This result is attributed to the system's high density and low temperature, i.e. high collision frequency, which allows experiments to be conducted in the gas dynamic trap regime.

From the set of initial experiments, we were also able to identify a number of required improvements. First, an external heating system needs to be added. We observed that increasing the source power is not effective to increase the electron temperature. Higher temperatures will be needed to simulate conditions closer to a tokamak boundary plasma. It may also be beneficial to consider varying collisionality in studying plasma physics. For these reasons, we will install an electron cyclotron heating system and ion cyclotron heating system in the near future.

Second, plasma stabilization will be required to enhance plasma performance. Previous studies showed that it was essential to suppress the MHD instabilities for better confinement (England *et al.* 2009; Ryutov *et al.* 2011; Qing *et al.* 2023). In the near future, we will scan the location of the collector to adjust the stability of the interchange mode. We will also utilize the vortex flow scheme (Beklemishev *et al.* 2010) to suppress the radial transport driven by MHD instabilities.

Third, to estimate the particle and energy confinement times, we need to improve the experimental conditions and measurements, as follows. In this study, we initially calculated the stored electron energy during the stationary period. To estimate the energy confinement time from the power balance equation, it is required to estimate the radiative energy loss and the loss due to collisions with neutrals as well as the energy stored

https://doi.org/10.1017/S0022377824000242 Published online by Cambridge University Press

in the plasma. For the radiative loss, although bremsstrahlung power is expected to be much lower than other loss mechanisms such as axial loss, line radiations also contribute to radiative loss. Therefore, radiative loss power should be checked using a bolometer in the future. To calculate the energy loss due to collisions with neutrals, the density of the metastable states of the neutral atom is necessary. We will utilize the collision–radiative model to calculate the density of the metastable states. To estimate the particle confinement time, we will develop diagnostics measuring particle flux at the expander chamber. In addition, the confinement time can be estimated from the decay time of the plasma when the source power is turned off. Although we observed a longer decay time in I_{sat} than the power decay time, we did not utilize this decay time to estimate the energy confinement time since the decay time of the source power ($\sim$0.6 ms) is similar to the decay time of I_{sat} ($\sim$1.6 ms) in the current system and the I_{sat} level, $\sim n_e T_e^{1/2}$, does not indicate either the exact particle or energy level. To analyse the confinement time in the decay period, the power decay time should be shorter than the estimated confinement time. We plan to add a switching circuit to actively control the current flow to the plasma source and shorten the decay time in the future. We will also install an interferometer and a diamagnetic loop for the plasma density and energy measurements, respectively. These diagnostics will be utilized to estimate the confinement time in the near future.

Acknowledgements

Editor Cary Forest thanks the referees for their advice in evaluating this article.

Funding

This work was supported by the National Research Foundation of Korea (NRF) funded by the Korean government (Ministry of Science and ICT) (RS-2023-00212124, RS-2022-00155956) and by an internal project funded by the Korea Advanced Institute of Science and Technology (KAIST) (N10230029, N10230137). I.K. gratefully acknowledges financial support from Khalifa University via the (internally funded) grants (FSI-2021-012/8474000352, CIRA-2021-064/8474000412).

Declaration of interests

The authors have no conflicts to disclose.

REFERENCES

ARAKAWA, H., INAGAKI, H. Y., SASAKI, M., KIN, F., HASAMADA, K., YAMASAKI, K., KOBAYASHI, T., YAMADA, T., NAGASHIMA, Y., FUJISAWA, A., *et al*. 2019 Ion temperature measurement by laser-induced fluorescence spectroscopy in panta. *IEEJ Trans. Electr. Electron. Engng* **14** (10), 1450–1454.

BAGRYANSKY, P.A., ANIKEEV, A.V., DENISOV, G.G., GOSPODCHIKOV, E.D., IVANOV, A.A., KOVALENKO, YU.V., MALYGIN, V.I., MAXIMOV, V.V., KOROBEINIKOVA, O.A., MURAKHTIN, S.V., *et al*. 2015 Overview of ECR plasma heating experiment in the GDT magnetic mirror. *Nucl. Fusion* **55** (5), 1–12.

BAGRYANSKY, P.A., CHEN, Z., KOTELNIKOV, I.A., YAKOVLEV, D.V., PRIKHODKO, V.V., ZENG, Q., BAI, Y., YU, J., IVANOV, A.A. & WU, Y. 2020 Development strategy for steady-state fusion volumetric neutron source based on the gas-dynamic trap. *Nucl. Fusion* **60** (3), 1–15.

BALDWIN, D.E. & LOGAN, B.G. 1979 Improved tandem mirror fusion reactor. *Phys. Rev. Lett*. **43** (18), 1318–1321.

BEKLEMISHEV, A.D., BAGRYANSKY, P.A., CHASCHIN, M.S., SOLDATKINA, E.I. 2010 Vortex confinement of plasmas in symmetric mirror traps. *Fusion Sci. Technol*. **57** (4), 351–360.

BURDAKOV, A.V. & POSTUPAEV, V.V. 2018 Multiple-mirror trap: a path from Budker magnetic mirrors to linear fusion reactor. *Phys. Uspekhi* **61** (6), 582–600.

CHEN, F.F. 2001 Langmuir probe analysis for high density plasmas. *Phys. Plasmas* **8** (6), 3029–3041.

CHEN, F.F. 2003 Langmuir Probe Diagnostics. in Proc. *IEEE-ICOPS Meeting*, Jeju, Republic of Korea, pp. 1–40.

DERBY, N. & OLBERT, S. 2010 Cylindrical magnets and ideal solenoids. *Am. J. Phys*. **78** (3), 229–235.

DIMOV, G.I. 2005 The ambipolar trap. *Phys. Uspekhi* **48** (11), 1129–1149.

ENDRIZZI, D., ANDERSON, J.K., BROWN, M., EGEDAL, J., GEIGER, B., HARVEY, R.W., IALOVEGA, M., KIRCH, J., PETERSON, E., PETROV, YU.V., *et al*. 2023 Physics basis for the Wisconsin HTS Axisymmetric Mirror (WHAM). *J. Plasma Phys*. **89** (5), 1–35.

ENGLAND, A.C., LEE, D.K., LEE, S.G., KWON, M., YOON, S.W., YASAKA, Y., SUGIMOTO, N., KATANUMA, I., YASHIRO, K. & IMAI, T. 2009 Mirror stabilization experiments in the Hanbit device. *Nucl. Fusion* **49** (12), 1–13.

EZUMI, N., IIJIMA, T., SAKAMOTO, M., NAKASHIMA, Y., HIRATA, M., ICHIMURA, M., IKEZOE, R, IMAI, T., KARIYA, T. & KATANUMA, I. 2019 Synergistic effect of nitrogen and hydrogen seeding gases on plasma detachment in the GAMMA 10/PDX tandem mirror. *Nucl. Fusion* **59** (6), 1–5.

FIKSEL, G., ALMAGRI, A.F., CRAIG, D., IIDA, M., PRAGER, S.C. & SARFF, J.S. 1996 High current plasma electron emitter. *Plasma Sources Sci. Technol*. **5** (1), 78–83.

HASTIE, R.J. & TAYLOR, J.B. 1964 Maximum plasma pressure for containment in magnetic fields with finite minima. *Phys. Lett*. **9** (3), 241–242.

IOFFE, M.S. & KADOMTSEV, B.B. 1970 Plasma containment in adiabatic traps. *Sov. Phys. Uspekhi* **13** (2), 225.

IVANOV, A.A., ANIKEEV, A.V., BAGRYANSKY, P.A., BOCHAROV, V.N., DEICHULI, P.P, KARPUSHOV, A.N, MAXIMOV, V.V., POD'MINOGIN, A.A., ROGOZIN, A.I., SALIKOVA, T.V., *et al*. 1994 Experimental study of curvature-driven flute instability in the gas-dynamic trap. *Phys. Plasmas* **1** (5), 1529–1535.

IVANOV, A.A. & PRIKHODKO, V.V. 2017 Gas dynamic trap: experimental results and future prospects. *Phys. Uspekhi* **60** (5), 509–533.

MOIR, R.W. & POST, R.F. 1969 Yin-yang minimum-|B| magnetic-field coil. *Nucl. Fusion* **9** (3), 243.

MORGAN, T.W., RINDT, P., VAN EDEN, G.G., KVON, V., JAWORKSI, M.A. & CARDOZO, N.J.L. 2017 Liquid metals as a divertor plasma-facing material explored using the Pilot-PSI and Magnum-PSI linear devices. *Plasma Phys. Control. Fusion* **60** (1), 1–11.

NAGORNYJ, V.P., RYUTOV, D.D. & STUPAKOV, G.V. 1984 Flute instability of plasma in a gas-dynamic trap. *Nucl. Fusion* **24** (11), 1421–1438.

OHNO, N. 2017 Plasma detachment in linear devices. *Plasma Phys. Control. Fusion* **59** (3), 1–9.

OHNO, N., NISHIJIMA, D., TAKAMURA, S., UESUGI, Y., MOTOYAMA, M., HATTORI, N., ARAKAWA, H., EZUMI, N., KRASHENINNIKOV, S., PIGAROV, A., *et al*. 2001 Static and dynamic behaviour of plasma detachment in the divertor simulator experiment NAGDIS-II. *Nucl. Fusion* **41** (8), 1055–1065.

POST, R.F. 1987 The magnetic mirror approach to fusion. *Nucl. Fusion* **27** (10), 1579–1739.

QING, L.I., GUANGHUI, Z., BAOMING, R., JIACHENG, Y., ZHIDA, Y. & XUAN, S. 2023 Experimental studies of cusp stabilization in Keda Mirror with AXisymmetricity (KMAX). *Plasma Sci. Technol*. **25** (2), 1–7.

RAJU, G.G. 2018 *Gaseous Electronics: Tables, Atoms, and Molecules*. CRC Press.

RALCHENKO, Y., JANEV, R.K., KATO, T., FURSA, D.V., BRAY, I. & DE HEER, F.J. 2008 Electron-impact excitation and ionization cross sections for ground state and excited helium atoms. *At. Data Nucl. Data Tables* **94** (4), 603–622.

RATHOD, P.J., ANITHA, V.P., SHOLAPURWALA, Z.H. & SAXENA, Y.C. 2014 A Guillemin type e pulse forming network as the driver for a pulsed, high density plasma source. *Rev. Sci. Instrum*. **85** (6), 1–7.

ROSE, C.R. 2015 Type-E pulse-forming-network theory and synthesis. In *Digest of Technical Papers International Pulsed Power Conference*, IEEE, pp. 1–6.

ROSENBLUTH, M.N. & LONGMIRE, C.L. 1957 Stability of plasmas confined by magnetic fields. *Ann. Phys.* (*NY*) **1** (2), 120–140.

https://doi.org/10.1017/S0022377824000242 Published online by Cambridge University Press

RYUTOV, D.D., BERK, H.L., COHEN, B.I., MOLVIK, A.W. & SIMONEN, T.C. 2011 Magneto-hydrodynamically stable axisymmetric mirrors. *Phys. Plasmas* **18** (9), 1–25.

SOLDATKINA, E.I., BAGRYANSKY, P.A. & SOLOMAKHIN, A.L. 2008 Influence of the radial profile of the electric potential on the confinement of a high-β two-component plasma in a gas-dynamic trap. *Plasma Phys. Rep*. **34**, 259–264.

SOUKHANOVSKII, V.A. 2017 A review of radiative detachment studies in tokamak advanced magnetic divertor configurations. *Plasma Phys. Control. Fusion* **59** (6), 1–12.

SUDNIKOV, A.V., IVANOV, I.A., INZHEVATKINA, A.A., LARICHKIN, M.V., LOMOV, K.A., POSTUPAEV, V.V., TOLKACHEV, M.S. & USTYUZHANIN, V.O. 2022 Plasma flow suppression by the linear helical mirror system. *J. Plasma Phys*. **88** (1), 1–16.

THAKUR, S.C., GOSSELIN, J.J., MCKEE, J., SCIME, E.E., SEARS, S.H. & TYNAN, G.R. 2016 Development of core ion temperature gradients and edge sheared flows in a helicon plasma device investigated by laser induced fluorescence measurements. *Phys. Plasmas* **23** (8), 1–10.

YAKOVLEV, D.V., SHALASHOV, A.G., GOSPODCHIKOV, E.D., MAXIMOV, V.V., PRIKHODKO, V.V., SAVKIN, V.YA., SOLDATKINA, E.I., SOLOMAKHIN, A.L. & BAGRYANSKY, P.A. 2018 Stable confinement of high-electron-temperature plasmas in the GDT experiment. *Nucl. Fusion* **58** (9), 1–7.

https://doi.org/10.1017/S0022377824000242 Published online by Cambridge University Press